Scattering angle dependence of temperature susceptivity of electron scattering in scanning transmission electron microscopy

Menglin Zhu, Jinwoo Hwang[*]

Department of Materials Science and Engineering, The Ohio State University, Columbus, OH 43210, USA

A B S T R A C T

The sensitivity of electron scattering to sample temperature (T) as a function of the scattering angle in scanning transmission electron microscopy (STEM) is investigated. Thermal vibration of atoms in crystal lattice results in attenuated Bragg reflections and a diffuse background in electron diffraction patterns, which have direct implications on STEM images. The scattering intensities at higher angle are known to be dominated by thermal diffuse scattering (TDS) and the column intensity is expected to have a negative correlation with increasing T because of the disrupted channeling, but the T susceptivity of the scattering intensity at smaller angles is less known. Our experiment shows that the T dependency of annular averaged diffraction intensity inverts its sign two times outside the direct beam, and the T sensitivity varies significantly as a function of scattering angle. The intensity shows a positive correlation with increasing T at the low to intermediate angular ranges before it returns to the negative correlation at the higher angle range. A reasonable agreement is found between the experimental data and multislice simulation data. Absorptive model is used to provide theoretical insights into the observed trends. Similar inversions of T dependency of column intensities are also observed in experimental and simulated atomic-resolution STEM images. The findings provide an important implication to the precise quantification of local T at high spatial resolution by optimizing the collection angles in STEM.

1. Introduction

Phonons can actively interact with incoming radiations and contribute to different kinds of scattering experiments, such as in Raman [1,2], X-ray [3,4], neutron [5,6], and electron [7–11] scatterings. Each of the techniques corresponds to a distinct part of the phonon spectrum and has been applied to study phonon characteristics in many scenarios [12]. Regardless of the type of radiations, their interactions with phonons are inelastic, meaning both the energy and momentum are changed after the scattering events. The same context applies to (scanning) transmission electron microscopy (S/TEM) where the incoming electrons are scattered by vibrating atoms, or lattices if the material is crystalline. Such inelastic interactions generally deplete the intensity of sharply peaked Bragg reflections from the periodic structure of the crystal and result in a diffuse background in between Bragg reflections, which is commonly known as the thermal diffuse scattering (TDS). The overall intensity of TDS is typically much lower than that of Bragg diffraction at lower scattering angles, and, therefore, it can be disregarded for general structure determination by diffraction indexing.

However, TDS has to be considered accurately in quantitative analysis of STEM images [13–15], or diffraction patterns for subtle information, such as the determination of charge-density distribution [16].

Various frameworks were developed to understand the complicated details in real space images or diffraction patterns induced by phonon scattering, including the absorptive TDS model [10,17], frozen phonon model [18], and quantum excitation of phonon (QEP) model [19]. Based on the evolution of theoretical understanding, TDS has been extensively studied in S/TEM. For example, absorptive potential has been numerically evaluated for different Bloch waves [20] and has proven its validity in quantitative interpretation of contrast in large-angle convergent beam electron diffraction patterns (CBED) [21]. Stobbs factor, the discrepancy in image contrast between theoretical and experimental data, could find its partial origination in TDS [22]. Kikuchi bands, arisen from inelastic scattering, have been demonstrated successfully in simulation using the frozen phonon model [7,18]. The sensitivity of electron scattering to phonons has also motivated many efforts in temperature (T) measurements using electron-energy loss spectroscopy (EELS) [23] and diffraction patterns [11,24] in S/TEM.
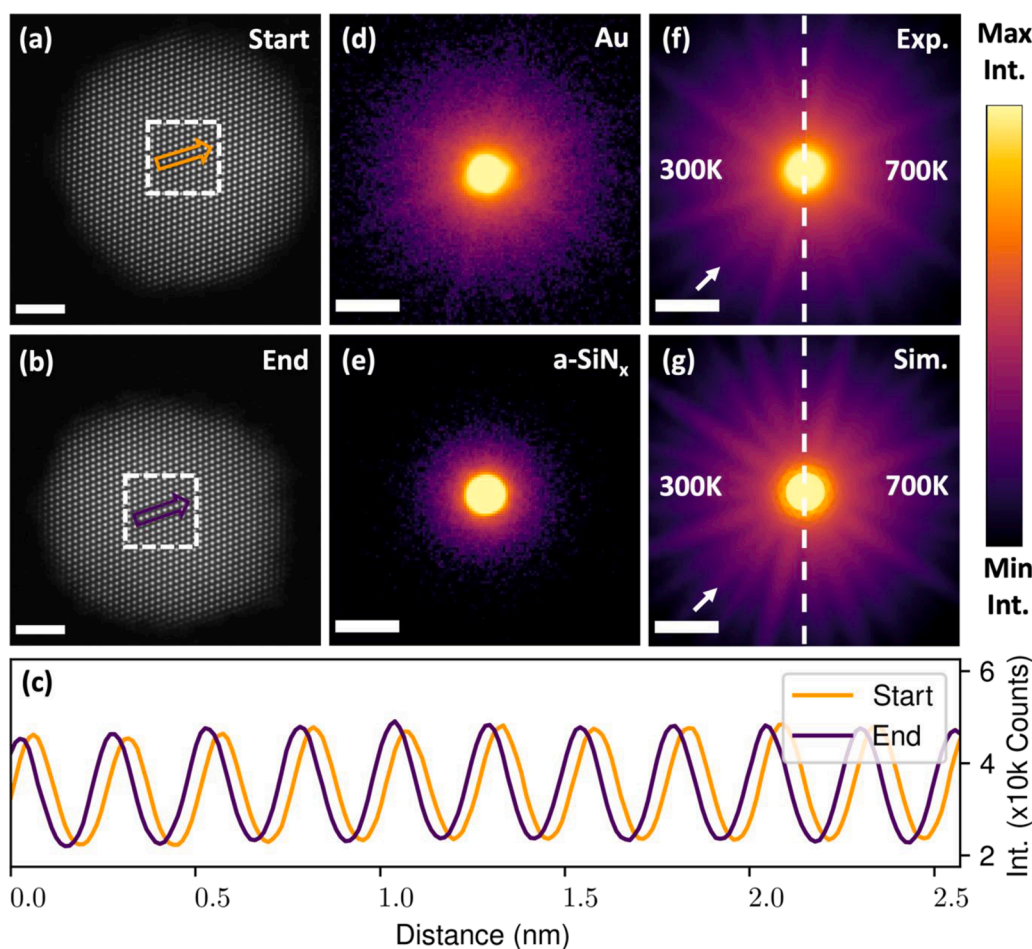

Fig. 1. HAADF image (a) at the start of the experiment and (b) at the end of the experiment. Scale bars in (a) and (b) corresponds to 2 nm. (c) Intensity line scan along columns indicated by the arrows in (a) and (b). Intensity are raw count readings from 16-bit image (0–65,536). Two profiles are offset on purpose for better visibility. Representative diffraction patterns, (d) at one probe position on Au, and (e) at one probe position on a-SiN$_x$. (f) Experimental PACBED pattern averaged over the area inside the white box shown in (a) and (b). Left half is collected at 300 K and right half at 700 K. (g) Simulated counterpart of (f). Fig. (d)–(g) are displayed on log scale for better virtualization of signals at higher angles, and the scale bars correspond to 3 Å^{-1}. The white arrows in (f) and (g) indicate the location of HOLZ line. The color bar applies to (d)–(g).

The advances mentioned above have made it possible to pursue the characterization of local *T* and thermal properties of materials at the length scales much smaller than what other large area diffraction, optical, or spectroscopic methods could achieve. However, challenges remain in probing the thermal scattering at the nanoscale, or even down to the atomic scale using high-precision S/TEM thermometry. EELS and diffraction analyses have pushed the spatial limit (and energy limit, in case of spectroscopy) of nano-thermometry, yet they still show limitations in spatial resolution and *T* precision, especially when it comes to determining how nanoscale structure affects the local thermal properties. In the case of STEM-EELS, for example, the intrinsic limit of spatial resolution is set by the plasmons delocalization length, which is sample dependent and typically on the scale of a few nanometers. Longer collection time or spatial averaging over tens of square nanometers [23] of the spectrums is sometimes necessary to get enough counts. A sophisticated curve fitting to the spectrums is also required to detect the minute shift of peaks, which is critical to the precision of *T* measurements. However, the peak positions in the EELS spectrum could be shifted by the presence of any non-uniformity, *e.g.*, defects, grain boundaries, or any interfaces included within the averaged area, which can substantially affect the precision of the measurement.

The attenuation of Bragg peaks and amplification of diffuse background in diffraction patterns was also explored to measure local *T*. The *T* dependency of the background was experimentally demonstrated in TEM mode, by measuring Bragg intensity [8] or performing TDS-EELS [25], but the spatial resolution is limited by the size of selective area aperture. Recently, the TDS background in between Bragg disks has also been evaluated using energy-filtered STEM-CBED patterns to measure local *T* [11] at length scale of about 5 nm. To achieve atomic resolution

in *T* determination, a convergence angle of around 10 mrad or larger should be used. Such a high convergence angle typically results in overlapping of the diffraction disks, leaving the intensity as an interplay between the peak attenuation and increase in the TDS background. The high angle annular dark field (HAADF) signals are known to be dominated by TDS [7,18,26], and expected to decrease with increasing *T* [27, 28] due to the disrupted channeling condition by atom vibrations. However, more detailed understanding of how the *T* sensitivity of electron scattering changes as a function of the scattering angle (in other words, *T* sensitivity of different STEM imaging modes), as well as optical parameters, is missing, which hinders the development of nanoscale thermometry to achieve even higher resolution and precision.

In this paper, we attempt to fill the gap by studying the use of a highly converged electron probe in STEM to measure *T* at the length scale of a unit cell level and atomic resolution with high *T* precision. Along with other recent advances in STEM, such as high brightness electron source and low drift stage, the important technical advantage that we utilize is the four-dimensional STEM (4D-STEM, 2D diffraction patterns from the 2D real space) [29–31]. With the advent of fast pixelated detector, the diffraction pattern up to high scattering angles at each probe position can be recorded in 4D-STEM experiments, unlike conventional STEM imaging, which only outputs the summation of electrons scattered to a certain range in diffraction space. Consequently, in 4D-STEM, the changes in low [32–34] and high [35–37] angle electron scatterings as a function of materials' characteristics or experimental conditions can be studied selectively or conjointly to reveal important properties. The detector we used is electron microscopy pixel array detector (EMPAD) from Thermofisher Scientific [38], which features high dynamic range (32 bit) and fast read-out speed. The linear

relationship between recorded intensity and the number of electrons ensures true quantification, therefore, the T dependency of electrons scattered to different angular ranges can be studied. In the following sections, we first show the annular averaged intensity of position averaged CBED (PACBED) acquired from the 4D-STEM data, which displays two inversions of the T dependency as a function of the scattering angle. The intensity shows a negative correlation with increasing T within the zero beam; then switches to a positive correlation in the low to intermediate angular range; and finally returns to a negative correlation in high angular range. The highest sensitivity is detected in a moderate scattering angle instead of high angles. Reasonable agreement with theoretical prediction is then demonstrated using QEP model, and the explanation of the inversion behavior is offered based on QEP and absorptive models. Such agreement shows the potential to quantitively measure T at unit cell resolution by PACBED pattern matching. Then, we advance the study to atomic scale by showing the T sensitivity of column intensity of images reconstructed from 4D-STEM data as a function of inner and outer collection angles. The good agreement between the simulated and experimental results shows the potential of T measurement at the atomic resolution using STEM images and provides guide for choosing the optimal collection angle with the highest T sensitivity.

2. Experimental data

2.1. 4D-STEM collection and processing of CBED patterns

Experimental data is collected using aberration-corrected Thermofisher Scientific Themis Z S/TEM operated under an acceleration voltage of 300 kV. The measured semi-convergence angle of the STEM probe is 18 mrad, giving a sub-angstrom probe size at Scherzer defocus. Beam current is limited to 40 pA with a pixel size of ~ 0.33 A^2 (dose rate $\sim 8 \times 10^8$ e/A^2sec) to give enough signals and prevent extra phonon excitations induced by beam heating [39]. EMPAD with 128×128 pixels is used to collect the CBEDs, with a real-space sampling of 256×256 probe positions over a $\sim 14 \times 14$ nm region and a dwell time of 1 ms. Gold (Au) nanoparticles from Ted Pella, Inc. with a nominal size of 10 nm are used, because the simple crystal structure and oxide-free surface reduces unknown variables in the analysis. The 4D-STEM data is spatially averaged over an area of several unit cells (white box in Fig. 1a and b) to acquire PACBED patterns (Fig. 1f) for analysis. In-situ heating of the sample is performed using DENS Solutions Wildfire holder and dedicated nano-chips, which features localized, fast, and low-drift heating. Each chip has a Joule spiral heater and electron transparent windows with about 30 nm thick of amorphous SiN_x (a- SiN_x) membrane as substrate. T read-out is based on the resistivity of spiral heater and is pre-calibrated by the manufacturer to ensure high accuracy.

Au nanoparticles are distributed sparsely on the a-SiN_x membrane. 4D-STEM datasets are collected from the exact same particle for each T starting at 700 K down to 300 K with a decreasing step size of 100 K. The HAADF images collected before and after the experiment (Fig. 1a and b) do not show any significant change in particle size caused by sublimation or beam radiation, except for the shrunk width along the vertical direction by about 1 nm. The asymmetric shape change along one direction can be understood as the sublimation at high T driven by low activation energy of certain facets [40–42]. Similar effects are less pronounced for the region of interest at the center of the particle (regions within the white boxes of Fig 1a and b), which is evidenced by the column intensities profiles (Fig. 1c) acquired along the arrows in Fig. 1a and b. The region in the white box is assumed to have a uniform thickness, and approximately 60×60 CBED patterns collected within this region are averaged to generate PACBED patterns for later analysis. The thickness measured independently using PACBED [32] before and after the experiment remains consistently at $\sim 7 \pm 0.5$ nm, which further confirms the negligible effect of sublimation or beam damage on the region of interest.

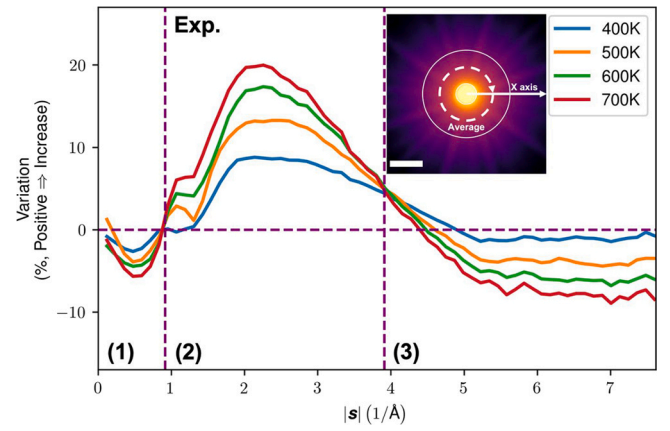Two example CBED patterns collected at different probe positions

Fig. 2. Variation (Eq. (1)) calculated for annular averaged intensity of PACBED collected experimentally at different T, as a function of the scattering vector magnitude, $|s|$. Positive values of variation indicate that I increases at the given temperature as compared to room temperature. Two vertical dashed lines approximately indicate where the inversion/crossover occurs. The inset is one representative PACBED pattern. The dashed line indicates how the annular averaging is done. Two solid circles correspond to the two locations where the inversion/crossover occurs.

(one from Au particle and the other from a-SiN_x) are shown in Fig. 1d and e, respectively. Two representative PACBED patterns collected at 300 and 700 K are shown in Fig. 1f along with the simulated counterparts (see Section 3.1 for details) in Fig. 1g. The effect of increasing T can already be identified from more diffuse background and blurrier Kikuchi lines at 700 K. Despite the overall good match between the experiment and simulation, some discrepancies can still be observed, such as the higher intensity right outside the zero beam and the missing high order Laue zone (HOLZ) line in the experimental data (white arrows in Fig. 1f *vs.* 1g). The discrepancy can be attributed to the following reasons. Firstly, the finite dimension and multi-facet shape of the nanoparticle is likely the major cause of missing HOLZ line in the experimental data. Imperfect crystallinity and inelastic scattering of Au nanoparticles could have also broadened the HOLZ line and made it less pronounced. Secondly, several factors are not considered in the simulation: (1) the non-uniform thickness of nanoparticle, which may slightly perturb the electron trajectory within the sample; (2) the background signal generated from the a-SiN_x membrane underneath, which is not included because there is a significant difference between average atomic numbers (~ 10 for a-SiN_x to ~ 78 for Au), and also because it is expected to be offset by itself in the normalization process later (Eq. (1)); (3) the incoherence of the source is not treated in Fig. 1g, which is typically done by convolving with a gaussian function [15]; (4) other inelastic scattering events such as plasmon and electronic excitations [43,44].

2.2. Variation of T dependency over scattering angles

To compare how the diffracted intensity changes with T at different diffraction angles, we first take the annular average of the PACBED patterns to get a 1D intensity profile as a function of the scattering vector magnitude, $|s|$, as shown in the inset of Fig. 2. The percentage variation of intensity at different T is then calculated by normalizing to the profile at room temperature (T_0) by

$$Variation\% = \frac{\overline{I_{T,|s|}} - \overline{I_{T_0,|s|}}}{\overline{I_{T_0,|s|}}} \times 100 \tag{1}$$

where $\overline{I_{T,|s|}}$ is the annular averaged diffraction intensity at T and a particular $|s|$. Variation greater than zero indicates that the annular averaged PACBED intensity at a given T and $|s|$ increases with respect to the corresponding value at room temperature (300 K).

The variation (Eq. (1)) calculated using the experimental data for each T (400 to 700 K) is shown in Fig. 2. The profiles show two cross-overs, once at ~1 Å^{-1} (coincides with the convergence angle), the second at ~ 4 Å^{-1}. Both are indicated by the vertical dashed lines in Fig. 2, as well as the solid circles in the inset. The profiles for all T invert signs simultaneously at the first crossover at ~1 Å^{-1}, but the inversion from positive to negative occurs successively after the second crossover at ~4 Å^{-1}. In regime (1) ($|s| \lesssim 1$ Å^{-1}), the variation has a negative sign indicating the intensity (I) decreases with increasing T. This is consistent with the general understanding of the attenuated Bragg diffraction by phonon scattering, which should occur for both the zero beam and the overlapping diffraction disks. In contrast, the positive variation in regime (2) ($1 \lesssim |s| \lesssim 4$ Å^{-1}) suggests that I increases with increasing T, which agrees with the increasing atomic column intensity that we previously measured using low-angle dark field STEM images from SrTiO$_3$ [45]. Two peaks can be identified in regime (2), a major one at ~ 2.3 Å^{-1} and a minor one at ~ 1.2 Å^{-1}. Lastly, in regime (3) ($|s| \gtrsim 4$ Å^{-1}), especially beyond HOLZ line ($|s| \gtrsim 6$ Å^{-1}), the sign of all profiles again turns negative and shows nearly uniform variation independent of $|s|$.

The inversion in the sign of variation is important to understand as it provides the potential for T measurement with high precision by template-matching of PACBED patterns with simulation or using atomic resolution images formed by electrons scattered to certain angular range. The negative sign of variation in HAADF region [*i.e.*, decrease of column intensity in atomic resolution images as T increases, corresponding to the regime (3) in Fig. 2] can be more naturally interpreted as, thermal vibrations disrupt the electron channeling and result in a less intense column in the image. However, the signs of the variation in the other two regimes, especially in (2), can be less intuitive. An explanation will be given based on QEP and absorptive models in the next section.

3. Theoretical understanding

Theoretical calculations based on multislice QEP model, which can export thermal and elastic scattered signals separately, are used to demonstrate the inversion behavior similar to the experimental results. The absorptive model is then used to provide a physical intuition on the mechanism of the inversion behavior.

3.1. QEP multislice model

In this section, a brief background of frozen phonon and QEP model will be given. Simulation based on multislice QEP model [19] with parameters resembling the experimental conditions will then be demonstrated, which shows similar inversion behavior observed in the experiment.

Frozen phonon model is developed based on the premise that each electron in the probe is elastically scattered by one vibrational configuration of the lattice due to the much higher velocity of the probing electron comparing to the vibration of atoms [18]. Thus, the final intensity is the incoherent summation of intensities scattered by each frozen phonon configuration. This model provides a more accurate prediction for both elastic and TDS intensity, although the inelastic nature of the scattering, *i.e.*, change of energy and momentum, is not taken into account [46]. A more rigorous treatment of phonon excitation in electron scattering is proposed by solving the wave functions of scattered electrons based on Born-Oppenheimer approximation, namely quantum excitation of phonons (QEP) model [19,47]. While QEP model is proven to generate identical numerical output as frozen phonon model [47], the quantum mechanical treatment enables the separated output of the contributions from elastic and TDS scattering, which can provide more insights about image formation.
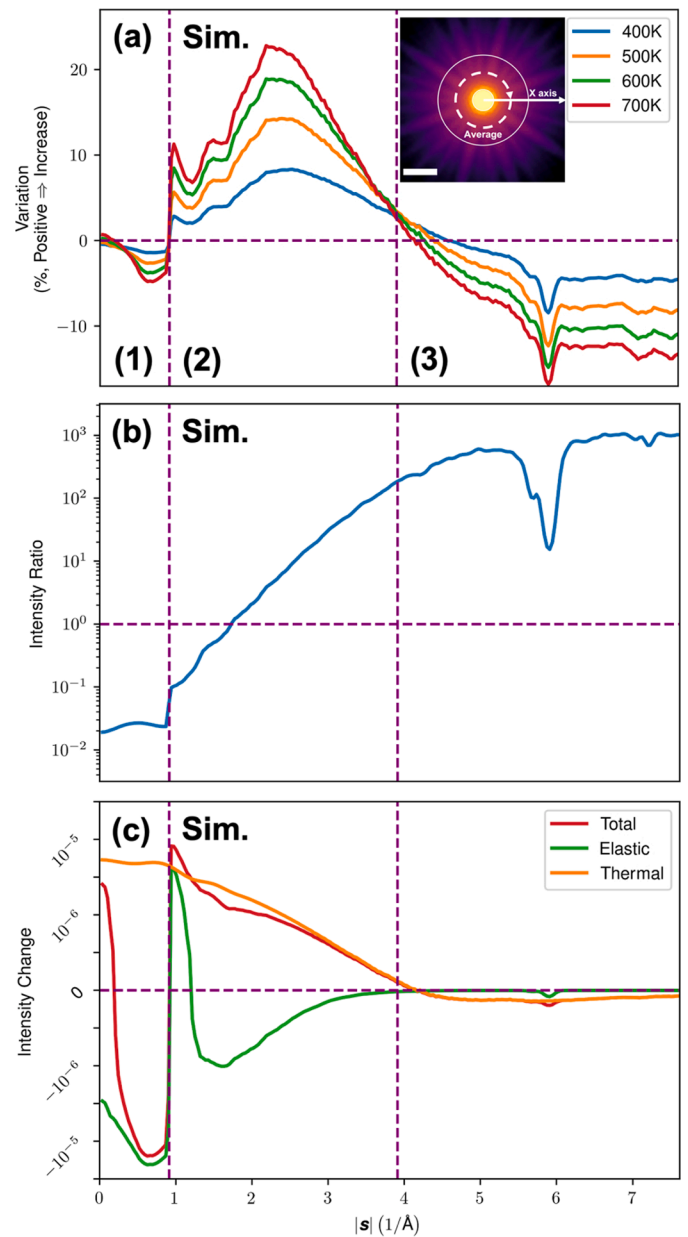

Fig. 3. (a) Variation (Eq. (1)) calculated for annular averaged intensity of PACBED simulated with QEP model with parameters resembling the experiment (sample thickness ~7 nm) at different T, as a function of the scattering vector magnitude, $|s|$. Positive values of variation indicate that I increases at the given temperature as compared to room temperature. Two vertical dashed lines indicate approximately where the inversion/crossover happens. The inset is one representative PACBED pattern. The dashed line demonstrates how the annular averaging is done. Two solid circles correspond to the two locations where the inversion/crossover happens. (b) The ratio between the elastic and TDS contributions ($I_{TDS}/I_{Elastic}$) to PACBED pattern at 300 K in QEP model as a function of the scattering vector magnitude, $|s|$. (c) Intensity change ($I_{700\ K} - I_{300\ K}$) for the elastic (green) and TDS (orange) parts of the total annular averaged PACBED intensity (red) (For interpretation of the references to color in this figure legend, the reader is referred to the web version of this article.).

Electron scattering simulation is performed with multislice QEP model (muSTEM) [19] to compare with the experimental data. The calculation is carried out with a 28.84×28.55 Å Au supercell (5×7 unit cells) along [110] zone axis on a 1025×1015 pixel array, giving the reciprocal space resolution of ~0.012 Å^{-1}. The band width limit of the simulation is checked to make sure there is no significant loss of electron

intensity. PACBED pattern is formed by averaging 88 CBED patterns sampled in one unit cell. At each probe position, 1000 frozen phonon configurations are used to ensure the convergence of the numerical result. Debye-Waller factors (DWFs) of Au are retrieved from literature [48]. Atomic displacements are assumed to follow the Einstein model. The assumption has some drawbacks (which will be addressed in later section), but it is shown to be robust enough to predict the phonon scatterings [49].

Same analysis done on experimental data as discussed in previous section is implemented on the calculated PACBED patterns. The simulated result in Fig. 3a shows the overall trend and peak/crossover positions that are consistent with the experimental data in Fig. 2. As compared to simulation, the experimental data in Fig. 2 is noisier and shows some quantitative discrepancies in the amount of variation. In addition to the experimental uncertainties mentioned in Section 2.1, the finite sampling of EMPAD, which gives an angular resolution of $0.119 \text{ Å}^{-1}/px$ as opposed to $0.012 \text{ Å}^{-1}/px$ in the simulation, could also contribute.

To understand the inversion behavior, it is important to first learn the nature of the signal at each regime. The diffraction intensity from the QEP model consists of the contributions from both the thermal scattering and the elastic scattering. The line profile in Fig. 3b shows the ratio between those two parts ($Ratio = I_{TDS}/I_{Elastic}$) for the calculated pattern at 300 K. The elastic contribution dominates within the direct beam $|s| \lesssim 1 \text{ Å}^{-1}$. An abrupt increase of the thermal contribution happens at $|s| \cong 1 \text{ Å}^{-1}$ where the first inversion takes place. The ratio then increases with larger $|s|$ and the thermal contribution starts to take over at $|s| \cong 2 \text{ Å}^{-1}$, where the greatest positive variation appears in Fig. 3a. The ratio reaches the maximum (order of $\sim 10^3$) at $|s| \cong 4.5 \sim 5 \text{ Å}^{-1}$, which roughly coincides with the locations where the positive to negative inversions happen in Fig. 3a. This observation highlights the role of the $I_{TDS}/I_{Elastic}$ ratio in the inversion behavior.

More details of the effects of thermal and elastic contributions on PACBED at elevated T can be seen in Fig. 3c. Here, the elastic and thermal components of the simulated PACBED intensity were compared between 300 and 700 K, along with the total (combined) intensity. The y-axis shows the difference of the annular averaged intensity between 700 and 300 K ($Difference = I_{700K, c} - I_{300K, c}$, where c denotes elastic, thermal, or total contribution). The red profile shows the total intensity change, which is equivalent to the summation of the green profile (elastic contribution) and the orange profile (thermal contribution). A positive value indicates the annular average intensity for the specific $|s|$ increases at 700 K compared to 300 K. The inversion of T dependency can be identified by the alternating sign of the red profile as a function of $|s|$. In the range $|s| \lesssim 1 \text{ Å}^{-1}$, the total annular averaged intensity decreases at 700 K. This is mainly due to the attenuation of elastic reflections (joint effects from the zero beam and lower ordered diffraction disks), as shown by the larger magnitude of the green profile comparing to the orange one. In regime (2), the attenuation of elastic scatterings becomes less significant, and an increase in total intensity at higher T is observed until the increase of thermal component (i.e., TDS background) at 700 K is large enough to offset the attenuation. However, in the range $1 \text{ Å}^{-1} \lesssim |s| \lesssim 1.2 \text{ Å}^{-1}$, there is a sharp increase in the elastic scattering in contrast to the other parts of regime (2), contributing to the minor peak at the same $|s|$ observed in Figs. 2 and 3a. A brief investigation with multislice simulation implied that this minor peak can be attributed to dynamical diffraction, but further investigation is needed to understand the details, which may be a subject of future work. In the range $|s| \gtrsim 4.5 \text{ Å}^{-1}$, the decrease in total intensity at 700 K results mostly from the decrease of thermally scattered signals, except for the region around the $|s| \cong 6 \text{ Å}^{-1}$ where the intensity shows a small dip due to the
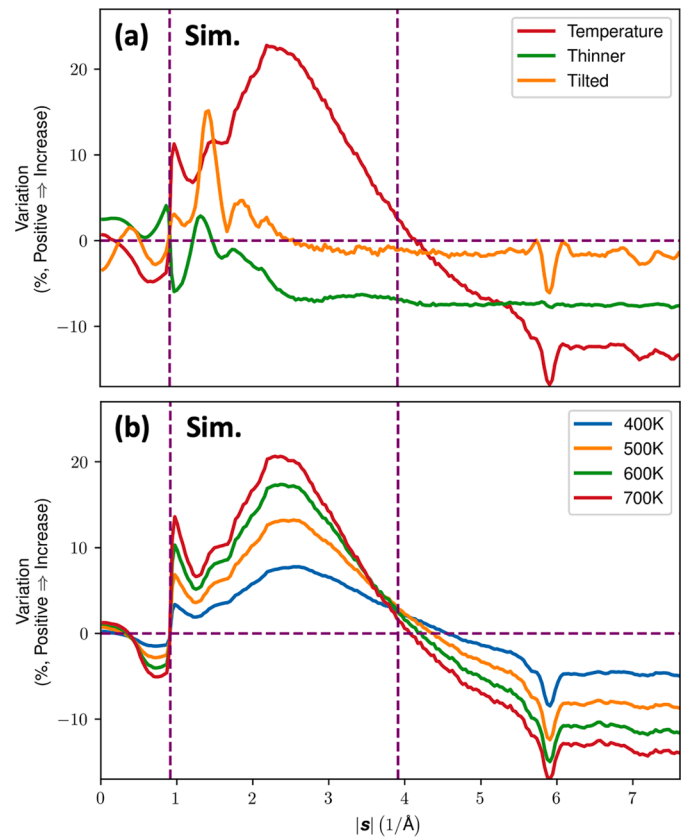

Fig. 4. (a) Variation (Eq. (1)) calculated for annular averaged intensity of PACBED simulated with QEP model as a function of the scattering vector magnitude, $|s|$, under the following conditions. Temperature: ~7 nm, 0 mrad tilt, 700 K; Thinner: ~6.4 nm, 0 mrad tilt, 300 K; and Tilted: ~7 nm, ~5 mrad tilt, 300 K. (b) Variation (Eq. (1)) calculated for annular averaged intensity of PACBED simulated with QEP model at different T as a function of the scattering vector magnitude, $|s|$. The model is 10% thinner (~6.4 nm) comparing to the one shown in Fig. 3a (~7 nm). Positive values of variation indicate that I increases at the given temperature as compared to room temperature. Two vertical dashed lines indicate approximately where the inversion/crossover happens (For interpretation of the references to color in this figure, the reader is referred to the web version of this article.).

influence from HOLZ line (which is elastic). The above-mentioned observations will find their explanations in the following section with absorptive model.

To further confirm that the trends observed is Figs. 2 and 3a are due to the contribution from T, the effects of other potential variables, such as sample thickness and tilt, will be briefly addressed here, as both are expected to influence T measurement with Debye-Waller effect [50,51]. Simulations are performed with the following conditions respectively: (1) ~7 nm thick, 0 mrad tilt, 300 K; (2) ~7 nm, 0 mrad, 700 K; (3) ~6.4 nm, 0 mrad, 300 K; and (4) ~7 nm, ~5 mrad, 300 K. Annular averaged line profiles of pattern (2)–(4) are normalized to (1) using Eq. (1) and the result is shown in Fig. 4a. Although 1 mrad tilt can be easily corrected using Ronchigram, 5 mrad sample mis-tilt is assumed to exaggerate the effect. As compared to the T induced variation (red line, which is the same as the red line in Fig. 3a), the variation induced by ~5 mrad tilt (orange line in Fig. 4a) appears to be relatively small when $|s| \gtrsim 1.5 \text{ Å}^{-1}$. A thinner sample (green line in Fig. 4a), on the other hand, decreases the intensity by ~10% when $|s| \gtrsim 1.5 \text{ Å}^{-1}$. A similar effect of thickness is observed in experimental data (not shown here). The results demonstrate that, while both the sample tilt and thickness can affect the intensity variation, their trends are vastly different from the one induced by T. This confirms T is the major source of intensity variations observed
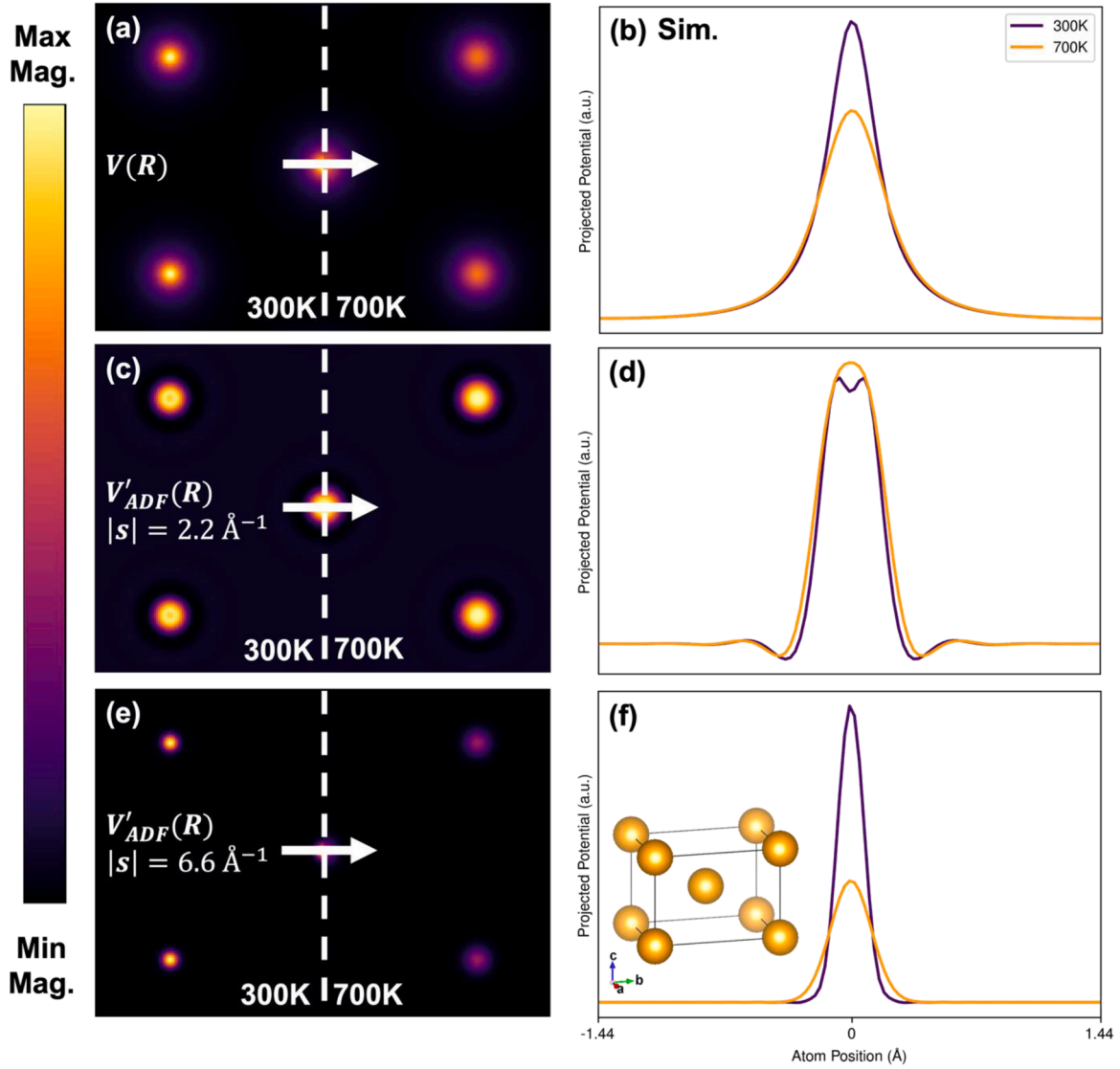
Fig. 5. (a) The projected real lattice potential is evaluated for Au model as shown in (f) inset based on the atomic form factor (Eqs. A.1 and A.2). Left side of the white dashed line is calculated at 300 K and right side at 700 K. Peak positions correspond to the locations of Au atoms. (b) The line profile of projected real lattice potential across one Au atom along the arrow in (a). (c) The projected ADF potential for Au with $|s| = 2.2$ Å^{-1} is evaluated based on the absorptive form factor with integration limit from $|s'| = 2.0$ Å^{-1} to $|s'| = 2.4$ Å^{-1} (Eqs. A.1, A.3 and A.4). (d) The line profile of projected ADF potential with $|s| = 2.2$ Å^{-1} across one Au atom along the arrow in (c). (e) The projected ADF potential for Au with $|s| = 6.6$ Å^{-1} is evaluated based on the absorptive form factor with integration limit from $|s'| = 6.4$ Å^{-1} to $|s'| = 6.8$ Å^{-1}. (f) The line profile of projected ADF potential with $|s| = 6.6$ Å^{-1} across one Au atom along arrow in (e). The inset shows the Au model for potential calculation. The a direction shown in the inset corresponds to [1–10] direction in FCC Au cell, b [001] and c [110]. The color bar applies to (a), (c), and (e).

in the experiment (Fig. 2). In addition, similar simulation and analysis as in Fig. 3a (~7 nm Au model) is done on a ~6.4 nm Au model as shown in Fig. 4b. All features preserve except for some intensity redistribution, which suggests that the general effect of T on electron scattering could be universal for samples dominated by kinematic diffractions.

3.2. Absorptive model

To incorporate the TDS contribution to HAADF images, Pennycook and Jesson introduced the ADF potential based on the absorptive model [26]. Here, we will follow their argument to provide a qualitative understanding of the inversion behavior observed in our experimental data, which supplements the interpretation provided using QEP model in the section above.

As transmitting through a perfect crystal, electron beam is scattered by the total crystal potential given by [20]

$$V_{total}(\mathbf{R}) = V(\mathbf{R}) + iV'(\mathbf{R}) \tag{2}$$

where $\mathbf{R}$ is 2-dimensional position vector in real space, $V(\mathbf{R})$ is the projected real lattice potential, $V'(\mathbf{R})$ is the projected absorptive potential. The real lattice potential, $V(\mathbf{R})$, represents the elastic scattering cross-section and its magnitude depends on the crystal structure and atomic form factors. The absorptive potential, $V'(\mathbf{R})$, represents the inelastic scattering cross-section (TDS in this case) and depends on the structure as well as absorptive form factors, which account for the intensity that should have been elastically scattered to certain angle ($|s|$) but is scattered to other angles instead due to the interactions with phonon. The magnitude of atomic and absorptive form factor has a direct implication on the relative contribution of elastic and thermal contribution to the total diffraction intensity. The slower decaying of absorptive form factor compared to atomic form factor with increasing
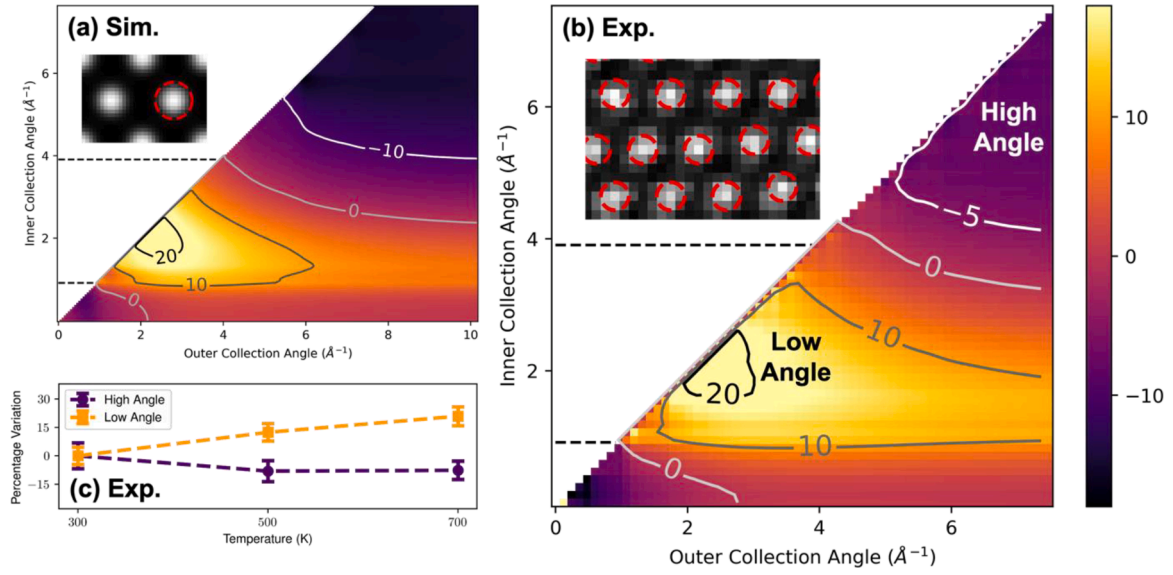
Fig. 6. (a) The inset shows one representative image reconstructed from simulated 4D-STEM data. Such images are reconstructed as a function of inner and outer collection angle at 300 K and 700 K, respectively. The intensity variation of the red circled column is taken between 700 and 300 K ($Variation\% = (I_{700\ K} - I_{300K})$ $/I_{300K} \times 100$) and plotted in (a). The two horizontal dashed lines indicate the location where inversion/crossover happens. (b) Similar analysis as in (a) is done on experimental data. The inset shows one image reconstructed from experimental data. The column intensity is the average of 5 nearest pixels around local maxima, as indicated by the red dashed circles (c) Images are reconstructed from experimental 4D-STEM data with $1.9 - 2.6$ Å^{-1} (low angle) and $5.9 - 7.1$ Å^{-1} (high angle) collection angle for 300 K, 500 K, and 700 K. The collection angles are labeled in (b). The percentage variation of column intensity with respect to 300 K is plotted as a function of T. The error bar indicates the standard deviation propagating from the non-uniform intensities measured from numerous columns. The color bar applies to (a) and (b).

$|s|$ (as explained in the Appendix) agrees with the observation in Fig. 3b that TDS plays a more important role comparing to elastic contribution as $|s|$ increases. On the other hand, ADF potential, $V'_{ADF}(\boldsymbol{R})$, is introduced based on the absorptive potential by only evaluating the absorptive form factor within the collection angle of ADF detector. Thus, $V'_{ADF}(\boldsymbol{R})$ accounts for the inelastically scattered intensity that is captured by the detector (derivation given in Appendix). In other words, a larger value of $V'_{ADF}(\boldsymbol{R})$ indicates a stronger thermal background in the detector range.

Based on the concept, we explain the inversion of variations observed in Figs. 2 and 3a. First, the projected real lattice potential for Au (model shown in Fig. 5f inset) is evaluated at 300 and 700 K, as shown in Fig. 5a. The line profile across one Au column is taken along the arrow in Fig. 5a and is shown in Fig. 5b. The real lattice potential smears out due to more intense thermal vibrations at higher T, leading to attenuation of elastic diffractions. This has a direct implication to the regime (1) in Figs. 2 and 3a, where the Bragg diffraction dominates.

Conversely, in regime (3) where HAADF detector typically locates, TDS should play a dominant role while the elastic counterpart is minute. To explain the T dependency in this range, $V'_{ADF}(\boldsymbol{R})$ is evaluated using absorptive form factor in a small range of $|s|$ (6.4 Å^{-1} to 6.8 Å^{-1}) to represent the TDS cross-section for $|s| = 6.6$ Å^{-1}, as shown in Fig. 5e (line profile in Fig. 5f). It can be noticed that $V'_{ADF}(\boldsymbol{R})$ is more localized compared to $V(\boldsymbol{R})$ and is smeared out by more intense atom vibrations at 700 K, as expected from previous study [26]. Consequently, the weaker potential results in a smaller TDS cross-section, and the annular averaged intensity is expected to decrease even though the total absorption increased.

Next, the idea of ADF potential is extended to regime (2), where both the TDS and elastically scattered electrons make moderate contributions to the total intensity. The ADF potential for $|s| = 2.2$ Å^{-1} is shown in Fig. 5c (line profile in Fig. 5d) based on absorption form factors in the range of $|s| = 2.0$ Å^{-1} to $|s| = 2.4$ Å^{-1}. It can be seen that the magnitude of ADF potential increases with higher T, leading to a higher TDS background intensity, which agrees with previous observation in STEM-

CBED pattern with low convergence angle [11]. This is because the total absorption increases at elevated T and more intensity is depleted from lower ordered Bragg disks into the background. For the specific experiment reported here, since convergence angle is large enough for diffraction disks to overlap, there will be a competition between the amplification of TDS background and the attenuation of Bragg reflections. In regime (2), Bragg conditions are less satisfied due to the larger excitation errors with increasing $|s|$. Thus, the intensities of Bragg reflections become weaker and so do the attenuations of Bragg reflections at higher T. At the same time, increasing T leads to a stronger TDS background. An inversion of T dependency happens at $|s| \gtrsim 1.2$ Å^{-1} when the attenuation of Bragg reflections is small enough to be compensated by the increase in TDS background. This argument can also explain the observation near the HOLZ line ($|s| \approx 6$ Å^{-1}) in Fig. 3c. Although the total intensity decreases at higher T consistently in regime (3), the one near HOLZ line shows a major contribution from attenuation of elastic scattering in contrast to TDS contribution of the other parts. This is because Bragg condition is perfectly satisfied at HOLZ line due to the curvature of Ewald's sphere, and the attenuation of strongly excited Bragg reflection makes an additional contribution to the decreasing intensity at higher T.

As explained above, the absorptive model provides a simple formulation and direct insights into the inversion behavior in the experiment (Fig. 2), which is also consistent with the observations in the QEP simulation result (Fig. 3). It should be noted that both absorptive and QEP models employed here assume that each atom vibrates independently following an Einstein model, and the angular redistribution is not evaluated accurately. However, this effect should be minute since the presented data is the annular averaged intensity. To apply it for quantitative thermal imaging in the future, more comprehensive modeling of atomic displacements can be used, for example. based on detailed phonon dispersion [7].

4. Direct imaging of temperature at the atomic scale

The result in Fig. 2 shows the potential to measure T by matching PACBED with simulation. Even though this approach can be immune to coherent aberrations [32], the resolution is limited to the unit cell level. In this section, we will advance the study of T sensitivity to atomic resolution. The intensity of STEM images can be seen as the summation of electrons scattered to certain angular ranges in diffraction space at each probe position. Thus, similar T dependency in Fig. 2 is also expected in STEM images. However, the conventional scintillator detector for STEM imaging typically covers a large angular range. The inversion behavior at different diffraction angles, which should also change with different material and experimental conditions (*e.g.*, convergence angle), makes it essential to use the right camera length to measure T with STEM imaging. Otherwise, the T induced intensity change can be compensated by the change with opposite sign in other $|s|$ ranges, which will reduce the T sensitivity or even reverse the contrast, as seen in some previous reports [52,53]. For example, if the detector is placed with inner angle at $|s| = 3 \text{ Å}^{-1}$ and outer collection angle at $|s| = 15 \text{ Å}^{-1}$, the positive ($3 \text{ Å}^{-1} \leq |s| \lessapprox 4.5 \text{ Å}^{-1}$) and negative ($4.5 \text{ Å}^{-1} \lessapprox |s| \leq 15 \text{ Å}^{-1}$) intensity variation is expected to compensate each other and degrades the T sensitivity.

A guideline for choosing the right collection angle for T measurement using atomic resolution STEM images is provided here. Real space image is reconstructed by integrating signals scattered to a certain angular range at each probe position for both simulated (one example in Fig. 5a inset) and experimental (one example in Fig. 5b inset) 4D-STEM datasets. The T sensitivity of STEM imaging is calculated as the relative change of column intensity at 700 K with respect to 300 K [*Variation*% $= (I_{700K} - I_{300K})/I_{300K} \times 100$] and is mapped as a function of inner and outer collection angles (y and x axes, respectively). A reasonable agreement can be found between experimental (Fig. 6b) and simulated (Fig. 6a) results. The maps show that optimal T sensitivity of STEM imaging can be achieved via two different settings of detector: first one [low angle (LA)] with inner angle ~2 Å^{-1} and outer angle ~3 Å^{-1}; second one [high angle (HA)] with inner angle ~6 Å^{-1}. The outer angle for the HA mode does not matter much since the variation of diffraction intensity is roughly uniform and independent of $|s|$ as shown in Figs. 2 and 3a. LA mode shows a higher T sensitivity but also changes dramatically as collection varies, therefore, careful calibration of the collection angles in simulation is required for quantifying local T. Also, the narrow collection range of LA mode is hard to achieve with typical scintillator detector. In contrast, HA mode shows a more uniform but smaller T sensitivity. Moreover, fewer electrons are scattered to HA, leading to a lower SNR. Real space images at 300, 500, and 700 K are reconstrued with HA and LA collecting conditions, and the percentage change of atomic column intensity with respect to 300 K is plotted in Fig. 6c, which shows a more significant variation with the LA mode.

Conclusion

Taking advantage of the high dynamic range of EMPAD, diffraction patterns at different T are collected up to high scattering angles with large convergence angle that is compatible with the atomic resolution imaging. The analysis of annular averaged PACBED intensity shows notable variation of T susceptivity as a function of scattering angle, including two inversions outside the direct beam. Such observations are shown to be consistent with QEP multisilce simulation data as well as the explanation based on the absorption model. The findings reported can lay the ground for T mapping with high resolution and precision via (1) matching PACBED maps with simulation data, and (2) atomic resolution images formed with electrons scattered to properly chosen angles.

Declaration of Competing Interest

The authors declare that they have no known competing financial interests or personal relationships that could have appeared to influence the work reported in this paper.

Acknowledgment

Appendix

We give the derivation of ADF potential following the idea by Pennycook and Jesson [26]. First, a brief background of the absorptive model will be provided. As transmitting through a perfect crystal, electron beam is scattered by the total crystal potential given by [20]

$$V_{total}(\boldsymbol{R}) = V(\boldsymbol{R}) + iV^{'}(\boldsymbol{R}) = \sum_{g} \left(V_g + iV_g^{'} \right) e^{-i\boldsymbol{g}\cdot\boldsymbol{r}}, \tag{A.1}$$

where $\boldsymbol{R}$ is 2-dimensional position vector in real space, $V(\boldsymbol{R})$ is the projected real lattice potential, $V^{'}(\boldsymbol{R})$ is the projected absorptive potential, and g is the reciprocal lattice vector. V_g is the Fourier component of the real lattice potential, which can be expressed as

$$V_g = -\frac{\hbar^2}{2m_0} \frac{4\pi}{\Omega} \sum_j f_j(\boldsymbol{s}) e^{-i\boldsymbol{g}\cdot\boldsymbol{r}_j} e^{-M_j s^2}, \tag{A.2}$$

where $f_j(\boldsymbol{s})$ is the atomic form factor of atom j, $\hbar$ is the reduced Planck constant, m_0 is electron rest mass, Ω is the unit cell volume, and r_j is the real space position vector of atom j in the unit cell. The effect of lattice vibration on real lattice potential is simply treated via the $e^{-M_j s^2}$ term, which includes the DWF of atom j, M_j, representing the root mean square displacements of atoms due to thermal vibrations [10]. This effectively dampens the Coulombic potential via a convolution with a Gaussian function. The formulation in Eq. A.2 neglects any inelastic scattering, which can be included by introducing an imaginary potential $V_g^{'}$, as shown in Eq. A.1. The imaginary potential accounts for the attenuation of elastic reflections by inelastic scattering and lays the groundwork for absorptive model [10]. $V_g^{'}$ can include any inelastic events, such as TDS, plasmon, and electronic excitations. However, the occurrence of TDS is essentially determined by the elastic scattering cross-section, while the others are controlled by inelastic scattering cross-section. The ratio of elastic to inelastic cross-section is large and scales with atomic number [20,54], thus only TDS contribution is considered here. $V_g^{'}$ can be represented with the same formulation as V_g in Eq. A.2 but replacing $f_i(\boldsymbol{s})$ with the absorptive form factor $f_i^{'}(\boldsymbol{s}, M)$:

$$V_g^{'} = -\frac{\hbar^2}{2m_0}\frac{4\pi}{\Omega}\sum_j{}^{'}f_j^{'}(\boldsymbol{s}, M)e^{-i\boldsymbol{g}\cdot\boldsymbol{r}_j}e^{-M_j s^2}, \tag{A.3}$$

and

$$f_j^{'}(\boldsymbol{s}, M) = \frac{2h}{m_0 v}\int d^2\boldsymbol{s}^{'} f_j(|\boldsymbol{s}^{'}|)f_j(|\boldsymbol{s}-\boldsymbol{s}^{'}|)\left[1 - e^{-2M_j\left(s^{'2}-\boldsymbol{s}\cdot\boldsymbol{s}^{'}\right)}\right], \tag{A.4}$$

where v is the speed of electron, and h is the Planck constant. For convenience, the vector geometry becomes symmetric by defining $\boldsymbol{s}^{'} \overset{def}{=} \boldsymbol{s}/2 + \boldsymbol{s}^{'}$, as shown below,

$$f_j^{'}(\boldsymbol{s}, M) = \frac{2h}{m_0 v}\int d^2\boldsymbol{s}^{'} f_j(|\boldsymbol{s}/2+\boldsymbol{s}^{'}|)f_j(|\boldsymbol{s}/2-\boldsymbol{s}^{'}|)\left[1 - e^{-2M_j\left(s^{'2}-s^2/4\right)}\right] \tag{A.5}$$

The dependence of TDS on elastic scattering cross-section is implied in the term $f_j(|\boldsymbol{s}/2+\boldsymbol{s}^{'}|)f_j(|\boldsymbol{s}/2-\boldsymbol{s}^{'}|)$. The implication of the formulation above is that as $|\boldsymbol{s}|$ increases, the exponential term, $1 - e^{-2M_j(s^{'2}-s^2/4)}$, increases, leading to slower decrease of the absorptive form factor, $f_j^{'}(\boldsymbol{s}, M)$, as compared to the elastic form factor, $f_j(\boldsymbol{s})$, which is also tabulated in previous work [55].

Next, we explain how the ADF potential is related to the formulation above. The value of the integrand, $f_j(|\boldsymbol{s}/2+\boldsymbol{s}^{'}|)f_j(|\boldsymbol{s}/2-\boldsymbol{s}^{'}|)[1 - e^{-2M_j(s^{'2}-s^2/4)}]$, in Eq. A.5 can be viewed as the intensity that should have been scattered to $\boldsymbol{s}$ is scattered to $\boldsymbol{s}^{'}$ due to interactions with phonons. Thus, the absorptive form factor, $f_j^{'}(\boldsymbol{s}, M)$ (Eq. A.5), calculated by integrating over the entire Ewald's sphere, accounts for the attenuation of the amplitude of elastic scattering. Consequently, absorptive model based on potential in Eq. A.1 only evaluates the wavefunctions of elastically scattered electrons, while thermal scattered ones are effectively absorbed by the imaginary potential, and their wavefunctions are not calculated. The absorptive model, therefore, fails to evaluate the angular redistribution of TDS and underestimates TDS background contribution in comparison to experimental images [13]. However, the total electron flux is conserved to a good approximation, meaning that the absorbed intensity is equal to the TDS intensity. The distribution of thermal scattered electrons can be inferred to some extent from the integrand of Eq. A.5 by restricting the integration within the ADF detector range [26], with the lower limit corresponding to the inner collection angle and the upper to the outer angle. Thus, the ADF potential evaluates the thermally scattered electrons that are captured by the detector. A stronger ADF potential indicates a larger cross-section for phonon scattering and higher TDS intensity within the detector range. Moreover, due to the nature of $V_g^{'}$, it has been shown that ADF potential is expected to be more localized for high collection angles and prone to the effect of thermal vibrations of atoms [26].

The concept of ADF potential is introduced based on the premise that the inelastically scattered electrons are redistributed tangential to the detector, and therefore negligible error results from ignoring the radial redistribution since the HAADF detector collects the signals in an annular geometry. This premise is also satisfied for the annular averaged data demonstrated here. Thus, we limit the integration to a small range of $|\boldsymbol{s}|$ and use it as a representative ADF form factor for the given $|\boldsymbol{s}|$. For example, the integrand is evaluated for $|\boldsymbol{s}|$ from $6.4\ \overset{\circ}{A}^{-1}$ to $6.8\ \overset{\circ}{A}^{-1}$ to calculate the ADF potential for $|\boldsymbol{s}| = 6.6\ \overset{\circ}{A}^{-1}$ as shown in Fig. 5e (line profile in Fig. 5f).

References

[1] S. Reich, C. Thomsen, Raman spectroscopy of graphite, Philos. Trans. R. Soc. A Math. Phys. Eng. Sci. 362 (2004) 2271–2288, https://doi.org/10.1098/rsta.2004.1454.

[2] J.A. Kash, J.C. Tsang, J.M. Hvam, Subpicosecond time-resolved Raman spectroscopy of LO phonons in GaAs, Phys. Rev. Lett. 54 (1985) 2151–2154, https://doi.org/10.1103/PhysRevLett.54.2151.

[3] M. Mohr, J. Maultzsch, E. Dobardžić, S. Reich, I. Milošević, M. Damnjanović, A. Bosak, M. Krisch, C. Thomsen, Phonon dispersion of graphite by inelastic x-ray scattering, Phys. Rev. B Condens. Matter Mater. Phys. 76 (2007), 035439, https://doi.org/10.1103/PhysRevB.76.035439.

[4] T. Ruf, J. Serrano, M. Cardona, P. Pavone, M. Pabst, M. Krisch, M. D'Astuto, T. Suski, I. Grzegory, M. Leszczynski, Phonon dispersion curves in wurtzite-structure GaN determined by inelastic X-ray scattering, Phys. Rev. Lett. 86 (2001) 906–909, https://doi.org/10.1103/PhysRevLett.86.906.

[5] H.F. Fong, B. Keimer, P.W. Anderson, D. Reznik, F. Doğan, I.A. Aksay, Phonon and magnetic neutron scattering at 41 meV in YBa$_2$Cu$_3$O$_7$, Phys. Rev. Lett. 75 (1995) 316–319, https://doi.org/10.1103/PhysRevLett.75.316.

[6] C.W. Li, O. Hellman, J. Ma, A.F. May, H.B. Cao, X. Chen, A.D. Christianson, G. Ehlers, D.J. Singh, B.C. Sales, O. Delaire, Phonon self-energy and origin of anomalous neutron scattering spectra in SnTe and PbTe thermoelectrics, Phys. Rev. Lett. 112 (2014), 175501, https://doi.org/10.1103/PhysRevLett.112.175501.

[7] D.A. Muller, B. Edwards, E.J. Kirkland E, J. Silcox, Simulation of thermal diffuse scattering including a detailed phonon dispersion curve, Ultramicroscopy 86 (2001) 371–380, https://doi.org/10.1016/S0304-3991(00)00128-5.

[8] A. Takaoka, K. Ura, Temperature measurement on micro-area of specimen in TEM by using thermal diffuse scattering effect, J. Electron Microsc. (Tokyo). 39 (1990) 69–70, https://doi.org/10.1093/oxfordjournals.jmicro.a050779.

[9] S.J.J. Pennycook, B. Rafferty, P.D.D. Nellist, Z-contrast imaging in an aberration-corrected scanning transmission electron microscope, Microsc. Microanal. 6 (2000) 343–352, https://doi.org/10.1007/s100050010045.

[10] C.R. Hall, P.B. Hirsch, Effect of thermal diffuse scattering on propagation of high energy electrons through crystals, Proc. R. Soc. Lond. Ser. A Math. Phys. Sci. 286 (1965) 158–177, https://doi.org/10.1098/rspa.1965.0136.

[11] G. Wehmeyer, K.C. Bustillo, A.M. Minor, C. Dames, Measuring temperature-dependent thermal diffuse scattering using scanning transmission electron microscopy, Appl. Phys. Lett. 113 (2018), https://doi.org/10.1063/1.5066111.

[12] P. Brüesch, Phonons: Theory and Experiments II, Springer Berlin Heidelberg, 1986, https://doi.org/10.1007/978-3-642-52263-5.

[13] J.M. Lebeau, S.D. Findlay, L.J. Allen, S. Stemmer, Quantitative atomic resolution scanning transmission electron microscopy, Phys. Rev. Lett. 100 (2008) 1–4, https://doi.org/10.1103/PhysRevLett.100.206101.

[14] J.M. LeBeau, S. Stemmer, Experimental quantification of annular dark-field images in scanning transmission electron microscopy, Ultramicroscopy 108 (2008) 1653–1658, https://doi.org/10.1016/j.ultramic.2008.07.001.

[15] J.M. LeBeau, S.D. Findlay, L.J. Allen, S. Stemmer, Standardless atom counting in scanning transmission electron microscopy, Nano Lett. 11 (2011) 310, https://doi.org/10.1021/nl1042215.

[16] J.M. Zuo, M. Kim, M. O'Keefe, J.C.H. Spence, Direct observation of d-orbital holes and Cu-Cu bonding in Cu$_2$O, Nature. 401 (1999) 49–52. www.nature.com.

[17] H. Yoshioka, Effect of inelastic waves on electron diffraction, 1957. 10.1143/JPSJ.12.618.

[18] R.F. Loane, P. Xu, J. Silcox, Thermal vibrations in convergent-beam electron diffraction, Acta Crystallogr. Sect. A. 47 (1991) 267–278, https://doi.org/10.1107/S0108767391000375.

[19] L.J. Allen, A.J. D'Alfonso, S.D. Findlay, Modelling the inelastic scattering of fast electrons, Ultramicroscopy 151 (2015) 11–22, https://doi.org/10.1016/j.ultramic.2014.10.011.

[20] D.M. Bird, Q.A. King, Absorptive form factors for high-energy electron diffraction, Acta Crystallogr. Sect. A. 46 (1990) 202–208, https://doi.org/10.1107/S0108767389011906.

[21] C.J. Rossouw, P.R. Miller, J. Drennan, L.J. Allen, Quantitative absorption corrections for electron diffraction: correlation between theory and experiment, Ultramicroscopy 34 (1990) 149–163, https://doi.org/10.1016/0304-3991(90)90069-X.

[22] A. Howie, Hunting the Stobbs factor, Ultramicroscopy 98 (2004) 73–79, https://doi.org/10.1016/j.ultramic.2003.08.002.

[23] M. Mecklenburg, W.A. Hubbard, E.R. White, R. Dhall, S.B. Cronin, S. Aloni, B.C. Regan, Nanoscale temperature mapping in operating microelectronic devices, Science (80-.). 347 (2015) 629–632. 10.1126/science.aaa2433.

[24] L. He, R. Hull, Quantification of electronphonon scattering for determination of temperature variations at high spatial resolution in the transmission electron microscope, Nanotechnology (2012) 23, https://doi.org/10.1088/0957-4484/23/20/205705.

[25] Z.L. Wang, A.T. Fisher, Electron energy-loss spectroscopy of high-angle thermal-diffuse-scattered electrons in TEM, Ultramicroscopy 48 (1993) 183–196, https://doi.org/10.1016/0304-3991(93)90181-V.

[26] S.J.J. Pennycook, D.E.E. Jesson, High-resolution Z-contrast imaging of crystals, Ultramicroscopy 37 (1991) 14–38, https://doi.org/10.1016/0304-3991(91)90004-P.

[27] Z. Yu, D.A. Muller, J. Silcox, Study of strain fields at a-Si/c-Si interface, J. Appl. Phys. 95 (2004) 3362–3371, https://doi.org/10.1063/1.1649463.

[28] S. Hillyard, J. Silcox, Detector geometry, thermal diffuse scattering and strain effects in ADF STEM imaging, Ultramicroscopy 58 (1995) 6–17, https://doi.org/10.1016/0304-3991(94)00173-K.

[29] C. Ophus, Four-dimensional scanning transmission electron microscopy (4D-STEM): from scanning nanodiffraction to ptychography and beyond, Microsc. Microanal. (2019) 563–582, https://doi.org/10.1017/S1431927619000497.

[30] M.W. Tate, P. Purohit, D. Chamberlain, K.X. Nguyen, R. Hovden, C.S. Chang, P. Deb, E. Turgut, J.T. Heron, D.G. Schlom, D.C. Ralph, G.D. Fuchs, K.S. Shanks, H. T. Philipp, D.A. Muller, S.M. Gruner, High dynamic range pixel array detector for scanning transmission electron microscopy, Microsc. Microanal. 22 (2016) 237–249, https://doi.org/10.1017/S1431927615015664.

[31] I. MacLaren, T.A. Macgregor, C.S. Allen, A.I. Kirkland, Detectors—The ongoing revolution in scanning transmission electron microscopy and why this important to material characterization, APL Mater. 8 (2020), 110901, https://doi.org/10.1063/5.0026992.

[32] J.M. LeBeau, S.D. Findlay, L.J. Allen, S. Stemmer, Position averaged convergent beam electron diffraction: theory and applications, Ultramicroscopy 110 (2010) 118–125, https://doi.org/10.1016/j.ultramic.2009.10.001.

[33] J. Hwang, J.Y. Zhang, J. Son, S. Stemmer, Nanoscale quantification of octahedral tilts in perovskite films, Appl. Phys. Lett. 100 (2012) 1–3, https://doi.org/10.1063/1.4714734.

[34] J. Hwang, J. Son, J.Y. Zhang, A. Janotti, C.G. Van de Walle, S. Stemmer, C.G. Van De Walle, S. Stemmer, Structural origins of the properties of rare earth nickelate superlattices, Phys. Rev. B Condens. Matter Mater. Phys. 87 (2013) 2–5, https://doi.org/10.1103/PhysRevB.87.060101.

[35] F.T.T. Huang, A. Gloter, M.W.W. Chu, F.C. Chou, G.J. Shu, L.K.K. Liu, C.H. Chen, C. Colliex, Scanning transmission electron microscopy using selective high-order Laue zones: three-dimensional atomic ordering in sodium cobaltate, Phys. Rev. Lett. 105 (2010) 1–4, https://doi.org/10.1103/PhysRevLett.105.125502.

[36] M. Nord, J. Barthel, C.S. Allen, D. McGrouther, A.I. Kirkland, I. MacLaren, Atomic resolution HOLZ-STEM imaging of atom position modulation in oxide heterostructures, Ultramicroscopy 226 (2021), 113296, https://doi.org/10.1016/J.ULTRAMIC.2021.113296.

[37] J.Y. Zhang, J. Hwang, B.J. Isaac, S. Stemmer, Variable-angle high-angle annular dark-field imaging: application to three-dimensional dopant atom profiling, Sci. Rep. 51 (5) (2015) 1–10, https://doi.org/10.1038/srep12419, 2015.

[38] Y. Jiang, Z. Chen, Y. Han, P. Deb, H. Gao, S. Xie, P. Purohit, M.W. Tate, J. Park, S. M. Gruner, V. Elser, D.A. Muller, Electron ptychography of 2D materials to deep sub-ångström resolution, Nature 559 (2018) 343–349, https://doi.org/10.1038/s41586-018-0298-5.

[39] R.F. Egerton, P. Li, M. Malac, Radiation damage in the TEM and SEM, Micron. 35 (2004) 399–409. 10.1016/j.micron.2004.02.003.

[40] M.A. Asoro, D. Kovar, P.J. Ferreira, *In situ* transmission electron microscopy observations of sublimation in silver nanoparticles, ACS Nano 7 (2013) 7844–7852, https://doi.org/10.1021/nn402771j.

[41] J. Li, Z. Wang, Y. Li, F.L. Deepak, *In situ* atomic-scale observation of kinetic pathways of sublimation in silver nanoparticles, Adv. Sci. 6 (2019), https://doi.org/10.1002/advs.201802131.

[42] Z.L. Wang, Transmission electron microscopy of shape-controlled nanocrystals and their assemblies, J. Phys. Chem. B 104 (2000) 1153–1175, https://doi.org/10.1021/jp993593c.

[43] A. Beyer, F.F. Krause, H.L. Robert, S. Firoozabadi, T. Grieb, P. Kükelhan, D. Heimes, M. Schowalter, K. Müller-Caspary, A. Rosenauer, K. Volz, Influence of plasmon excitations on atomic-resolution quantitative 4D scanning transmission electron microscopy, Sci. Rep. 10 (2020) 1–15, https://doi.org/10.1038/s41598-020-74434-w.

[44] J. Barthel, M. Cattaneo, B.G. Mendis, S.D. Findlay, L.J. Allen, Angular dependence of fast-electron scattering from materials, Phys. Rev. B. 101 (2020) 1–9, https://doi.org/10.1103/PhysRevB.101.184109.

[45] M. Zhu, J. Hwang, Quantification of thermal interface resistance using atomic scale Debye-Waller thermometry, Microsc. Microanal. 26 (2020) 960–962, https://doi.org/10.1017/s1431927620016499.

[46] D. Van Dyck, Is the frozen phonon model adequate to describe inelastic phonon scattering? Ultramicroscopy 109 (2009) 677–682, https://doi.org/10.1016/j.ultramic.2009.01.001.

[47] B.D. Forbes, A.V. Martin, S.D. Findlay, A.J. D'Alfonso, L.J. Allen, Quantum mechanical model for phonon excitation in electron diffraction and imaging using a Born-Oppenheimer approximation, Phys. Rev. B Condens. Matter Mater. Phys. 82 (2010) 1–8, https://doi.org/10.1103/PhysRevB.82.104103.

[48] L.M. Peng, G. Ren, S.L. Dudarev, M.J. Whelan, Debye-Waller factors and absorptive scattering factors of elemental crystals, Acta Crystallogr. 52 (1996) 456–470, https://doi.org/10.1107/S010876739600089X.

[49] B.D. Forbes, L.J. Allen, Modeling energy-loss spectra due to phonon excitation, Phys. Rev. B 94 (2016) 1–9, https://doi.org/10.1103/PhysRevB.94.014110.

[50] E.J. VandenBussche, D.J. Flannigan, D.R. Cremons, D.J. Flannigan, Sources of error in Debye-Waller-effect measurements relevant to studies of photoinduced structural dynamics, Ultramicroscopy 196 (2019) 111–120, https://doi.org/10.1016/j.ultramic.2018.10.002.

[51] D.R. Cremons, D.J. Flannigan, Direct *in situ* thermometry: variations in reciprocal-lattice vectors and challenges with the Debye-Waller effect, Ultramicroscopy 161 (2016) 10–16, https://doi.org/10.1016/j.ultramic.2015.10.022.

[52] M. Libera, J.A. Ott, K. Siangchaew, Temperature-dependent high-angle electron scattering from a phase-separated amorphous Ge-Te thin film, Ultramicroscopy 63 (1996) 81–91, https://doi.org/10.1016/0304-3991(96)00021-6.

[53] R.R. Vanfleet, D.P. Basile, T.I. Kamins, J. Silcox, R.S. Williams, Silicon-germanium interdiffusion and interfaces in self-assembled quantum dots, Appl. Phys. A Mater. Sci. Process. 86 (2007) 1–9, https://doi.org/10.1007/s00339-006-3724-8.

[54] L.J. Allen, S.D. Findlay, M.P. Oxley, C.J. Rossouw, Lattice-resolution contrast from a focused coherent electron probe, Part I, Ultramicroscopy. 96 (2003) 47–63, https://doi.org/10.1016/S0304-3991(02)00380-7.

[55] G. Radi, Complex lattice potentials in electron diffraction calculated for a number of crystals, Acta Crystallogr. Sect. A. 26 (1970) 41–56, https://doi.org/10.1107/S0567739470000050.